How to cite: *Angew. Chem. Int. Ed.* **2024**, *63*, e202320091
doi.org/10.1002/anie.202320091

Coordination Polymers

Control of the Hydroquinone/Benzoquinone Redox State in High-Mobility Semiconducting Conjugated Coordination Polymers

Xing Huang[+], Yang Li[+], Shuai Fu[+], Chao Ma, Yang Lu, Mingchao Wang, Peng Zhang, Ze Li, Feng He, Chuanhui Huang, Zhongquan Liao, Ye Zou, Shengqiang Zhou, Manfred Helm, Petko St. Petkov, Hai I. Wang, Mischa Bonn, Jian Li, Wei Xu,* Renhao Dong,* and Xinliang Feng**

Abstract: Conjugated coordination polymers (c-CPs) are unique organic–inorganic hybrid semiconductors with intrinsically high electrical conductivity and excellent charge carrier mobility. However, it remains a challenge in tailoring electronic structures, due to the lack of clear guidelines. Here, we develop a strategy wherein controlling the redox state of hydroquinone/benzoquinone (HQ/BQ) ligands allows for the modulation of the electronic structure of c-CPs while maintaining the structural topology. The redox-state control is achieved by reacting the ligand TTHQ (TTHQ = 1,2,4,5-tetrathiolhydroquinone) with silver acetate and silver nitrate, yielding Ag_4TTHQ and Ag_4TTBQ (TTBQ = 1,2,4,5-tetrathiolbenzoquinone), respectively. In spite of sharing the same topology consisting of a two-dimensional Ag–S network and HQ/BQ layer, they exhibit different band gaps (1.5 eV for Ag_4TTHQ and 0.5 eV for Ag_4TTBQ) and conductivities (0.4 S/cm for Ag_4TTHQ and 10 S/cm for Ag_4TTBQ). DFT calculations reveal that these differences arise from the ligand oxidation state inhibiting energy band formation near the Fermi level in Ag_4TTHQ. Consequently, Ag_4TTHQ displays a high Seebeck coefficient of 330 μV/K and a power factor of 10 $\mu W/m \cdot K^2$, surpassing Ag_4TTBQ and the other reported silver-based c-CPs. Furthermore, terahertz spectroscopy demonstrates high charge mobilities exceeding 130 $cm^2/V \cdot s$ in both Ag_4TTHQ and Ag_4TTBQ.

Introduction

Conjugated coordination polymers (c-CPs) and conjugated metal–organic frameworks (c-MOFs) represent a burgeoning class of crystalline electronic materials.[1] They are made from metal centers and electron-rich π-conjugated planar ligands with multiple pairs of ortho-substituted donor groups. Notable examples include 2,3,6,7,10,11-hexahydrox-

[*] Dr. X. Huang,[+] Dr. S. Fu,[+] Dr. Y. Lu, Dr. M. Wang, P. Zhang, Dr. C. Huang, Prof. X. Feng
Center for Advancing Electronics Dresden (cfaed), Faculty of Chemistry and Food Chemistry, Technische Universität Dresden
Dresden 01062, Germany
E-mail: xinliang.feng@tu-dresden.de

Dr. X. Huang,[+] Prof. X. Feng
Max Planck Institute of Microstructure Physics
Halle (Saale) 06120, Germany

Dr. Y. Li,[+] Z. Li, F. He, Y. Zou, Prof. W. Xu
Laboratory of Organic Solids, Institute of Chemistry Chinese Academy of Science
Beijing 100190, China
E-mail: wxu@iccas.ac.cn

Dr. S. Fu,[+] Prof. H. I. Wang, Prof. M. Bonn
Max Planck Institute for Polymer Research
Mainz 55128, Germany

C. Ma, Prof. J. Li
State Key Laboratory of Coordination Chemistry, School of Chemistry and Chemical Engineering, Nanjing University
Nanjing, Jiangsu 210023, China
E-mail: jian.li@nju.edu.cn

Dr. Z. Liao
Fraunhofer Institute for Ceramic Technologies and Systems (IKTS)
Dresden 01109, Germany

Dr. S. Zhou, Dr. M. Helm
Institute of Ion Beam Physics and Materials Research, Helmholtz-Zentrum Dresden-Rossendorf
Dresden 01328, Germany

Dr. P. S. Petkov
Faculty of Chemistry and Pharmacy, University of Sofia,
Sofia 1164, Bulgaria

Prof. H. I. Wang
Nanophotonics, Debye Institute for Nanomaterials Science, Utrecht University
3584 CC Utrecht, The Netherlands

Prof. R. Dong
Key Laboratory of Colloid and Interface Chemistry of the Ministry of Education, School of Chemistry and Chemical Engineering,
Shandong University
Jinan, 250100 China
E-mail: renhaodong@sdu.edu.cn

[+] These authors contributed equally to this work

ytriphenylene (HHTP),[2] 2,3,6,7,10,11- hexaaminotriphenylene (HATP),[3] and benzenehexathiol (BHT).[4] The strong π-*d* conjugation in c-CPs endows them with high charge mobility[5] and excellent electrical conductivity.[6] Furthermore, c-CPs possess unlimited molecular design space, rich structural topology diversity, and customizable porosity,[7] which make them functional semiconductors for potential electronic applications, such as field-effect transistors,[6a,8] gas sensors,[9] spintronics,[10] photodetectors,[11] quantum sensors,[12] and thermoelectrics.[13] The broader application scenarios and enhanced performance of c-CPs largely depend on their electronic band structures, whose precise tuning remains a significant challenge. In recent years, various synthetic strategies have been explored to exert control over the electronic structures of c-CPs and c-MOFs.[14] One such approach, atomic alloying,[14a] involves blending two different metal ions in the isostructural semiconducting c-CPs, allowing the band gap to be adjusted within a relatively small range (0.3–0.7 eV). Another method involves utilizing mixed ligands with similar topology but different substitution groups (e.g., 2,3,6,7,10,11-hexaaminotriphenylene (amino group) and 2,3,6,7,10,11-hexthioltriphenylene (thiol group)) within isostructural c-MOFs, which can also influence the electronic band structure.[15] Additionally, redox regulation has been shown to open the energy gap of metallic c-CPs.[14b–d,f] For instance, Ag_5BHT is treated with the redox reagent $LiBHEt_3$, resulting in a band gap observable by Ultraviolet Photoelectron Spectroscopy (UPS).[14d] Nevertheless, the underlying mechanism by which redox regulation modulates the physical properties of c-CPs remains unclear, largely due to the lack of precise elucidation of the structural evolution before and after the chemical treatment.

Inspired by the considerable influence of the oxidation state of conjugated molecules on their energy levels, here we demonstrate a novel strategy to manipulate the electronic band structure of c-CPs without altering the structural topology. Specifically, we achieve this by controlling the redox state of the hydroquinone/benzoquinone ligand during the synthesis process (Figure 1a, b). Two semiconducting c-CPs, namely Ag_4TTHQ (TTHQ = 1,2,4,5-tetrathiolhydroquinone) and Ag_4TTBQ (TTBQ = 1,2,4,5-tetrathiolbenzoquinone), were synthesized using TTHQ with silver acetate and silver nitrate, respectively. During the formation of Ag_4TTBQ, TTHQ underwent oxidation by the dilute nitric acid formed in situ before participating in the coordination reaction. Although both compounds have the same structural topology, Ag_4TTHQ exhibits a significantly larger band gap (1.5 eV vs. 0.5 eV for Ag_4TTBQ) and lower electrical conductivity than Ag_4TTBQ. Density Functional Theory (DFT) calculations suggest that the observed differences are triggered by the presence of an energy band near the Fermi level, which the oxidation state of the ligand can modulate. Consequently, Ag_4TTHQ displays an order of magnitude higher Seebeck coefficient (330 μV/K) and 2.5-fold higher thermoelectric power factor (10 $\mu W/m \cdot K^2$) than Ag_4TTBQ, surpassing all other reported silver-based coordination polymers (10^{-4} to 2 $\mu W/m \cdot K^2$). In addition, ultrafast terahertz (THz) spectroscopy reveals high charge carrier mobilities of 137 ± 7 $cm^2/(V \cdot s)$ and 130 ± 9 $cm^2/(V \cdot s)$ for Ag_4TTHQ and Ag_4TTBQ, respectively, as a result of their similar charge scattering times and small electron-hole effective masses. Our study highlights the fine-tuning of the electrical properties of c-CPs through redox-state control of the ligand, opening avenues for high-performance thermoelectric and electronic applications.

Results and Discussion

We carried out the coordination reaction between TTHQ and silver ions through two distinct synthetic routes to prepare silver-based c-CPs with different oxidation states (Figure 1b, synthesis details can be found in Supporting Information): 1) the one-pot reaction between TTHQ and silver acetate (AgOAc, $OAc^- = CH_3COO^-$) in a degassed methanol solution yielded Ag_4TTHQ; 2) the interfacial reaction between the aqueous solution of silver nitrate ($AgNO_3$) and the chlorobenzene solution of TTHQ produced Ag_4TTBQ. Once Ag ions react with thiol-based ligands, free protons (H^+) are usually substituted by the metal ions and released into the solution.[14d] In this respect, using $AgNO_3$ as the silver source leads to the in situ formation of dilute nitric acid due to the presence of H^+, which could further oxidize TTHQ into TTBQ.[16] In contrast, when AgOAc is employed as the silver source, acetic acid without oxidation ability is produced. Consequently, TTHQ would maintain its original oxidation state during the reaction. In conclusion, the rational selection of silver sources regulates the oxidation state evolution of the ligands and triggers different coordination reactions (Figure 1b). As a control experiment, solution synthesis of $AgNO_3$ and TTHQ in degassed methanol resulted in a mixture of Ag_4TTBQ and Ag_4TTHQ (detail in Supporting Information).

The as-prepared Ag_4TTHQ and Ag_4TTBQ samples present different colors: the well-ground Ag_4TTBQ powder was black with a metallic luster, while the Ag_4TTHQ powder was dark brown (Figure S1). The UV/Vis-Near IR absorption spectra (Figure 1c) show that Ag_4TTBQ exhibits much broader absorption than Ag_4TTHQ, indicating that Ag_4TTBQ has a smaller optical band gap (E_{opt}). The optical absorption edge of Ag_4TTHQ is located in the UV/Vis range (close to 800 nm), and its E_{opt} is calculated to be 1.5 eV based on the Tauc-plot analysis (Figure 1d). In contrast, Ag_4TTBQ has an absorption edge in the Near-IR region (up to 1400 nm), with a derived E_{opt} of 0.5 eV. The large difference in E_{opt} indicates the discrepancy in the electronic band structure between Ag_4TTHQ and Ag_4TTBQ.

To confirm the different oxidation states of ligands in these c-CPs, the IR and Raman spectra of Ag_4TTBQ, Ag_4TTHQ, and H_6TTHQ are compared, as shown in Figures 1e and 1f. The strong peaks at 2500 cm^{-1} and 3360 cm^{-1} in the IR spectrum of H_6TTHQ correspond to thiol and hydroxy groups, respectively. The absence of thiol group signals in both Ag_4TTBQ and Ag_4TTHQ indicates that all thiol groups were deprotonated and participated in the formation of c-CPs. Notably, a strong signal originating

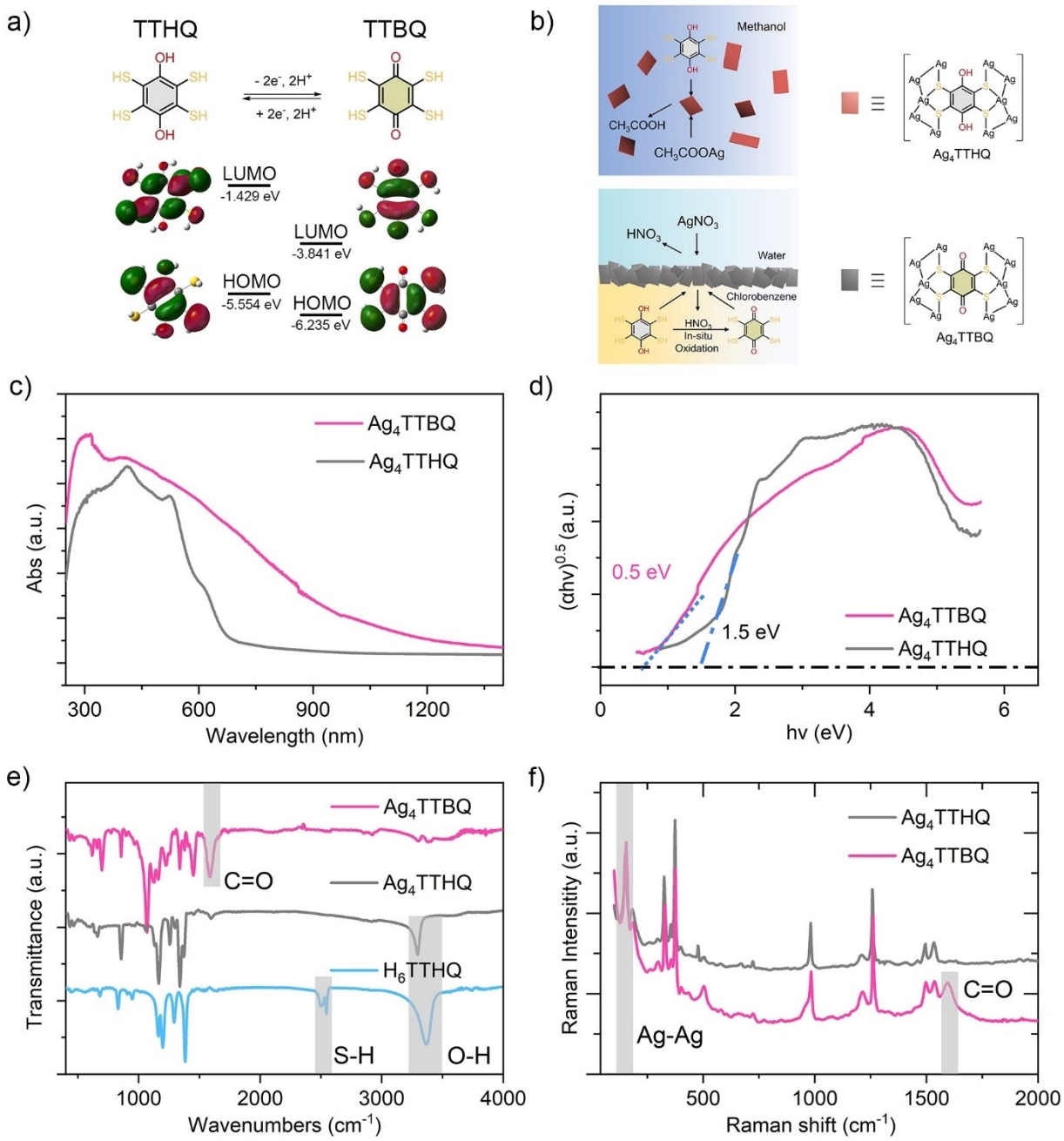

Figure 1. a) Redox couple between 2,3,5,6-tetrathiolhydroquinone (TTHQ) and 2,3,5,6-tetrathiol-1,4-benzenequinone (TTBQ); b) Synthetic routes towards Ag_4TTHQ and Ag_4TTBQ. During the interfacial synthesis of Ag_4TTBQ, in situ generated HNO_3 promotes the oxidation of TTHQ into TTBQ. (c) Comparison of the absorption spectra of Ag_4TTBQ and Ag_4TTHQ, along with their corresponding Tauc plots (d). (e) Comparison of IR spectra of Ag_4TTBQ, Ag_4TTHQ, and original H_6TTHQ ligand. (f) Raman spectra of Ag_4TTBQ and Ag_4TTHQ.

from hydroxy groups (~3300 cm^{-1}) remains visible in the IR spectrum of Ag_4TTHQ, whereas it is not identified in Ag_4TTBQ, indicating the presence of unbound hydroxy groups in Ag_4TTHQ. The hydroxyl group signal of Ag_4TTHQ is red-shifted and narrower than that of H_6TTHQ due to the formation of weak Ag–O coordination bonds and fewer hydrogen bonds. Furthermore, a sharp peak is observed at approximately 1600 cm^{-1} in the IR and Raman spectra of Ag_4TTBQ, which can be assigned to the stretching signal of the C=O bond; whereas this feature is absent in the spectra of Ag_4TTHQ. These results confirm that the deprotonation levels of the ligands in Ag_4TTHQ and Ag_4TTBQ are different due to the oxidation of TTHQ into TTBQ during the formation of Ag_4TTBQ.

To gain insights into the influence of ligand oxidation state on the resultant c-CP structure, atomic-precise structural characterization was performed. Figure 2a compares the synchrotron PXRD patterns of Ag_4TTBQ and

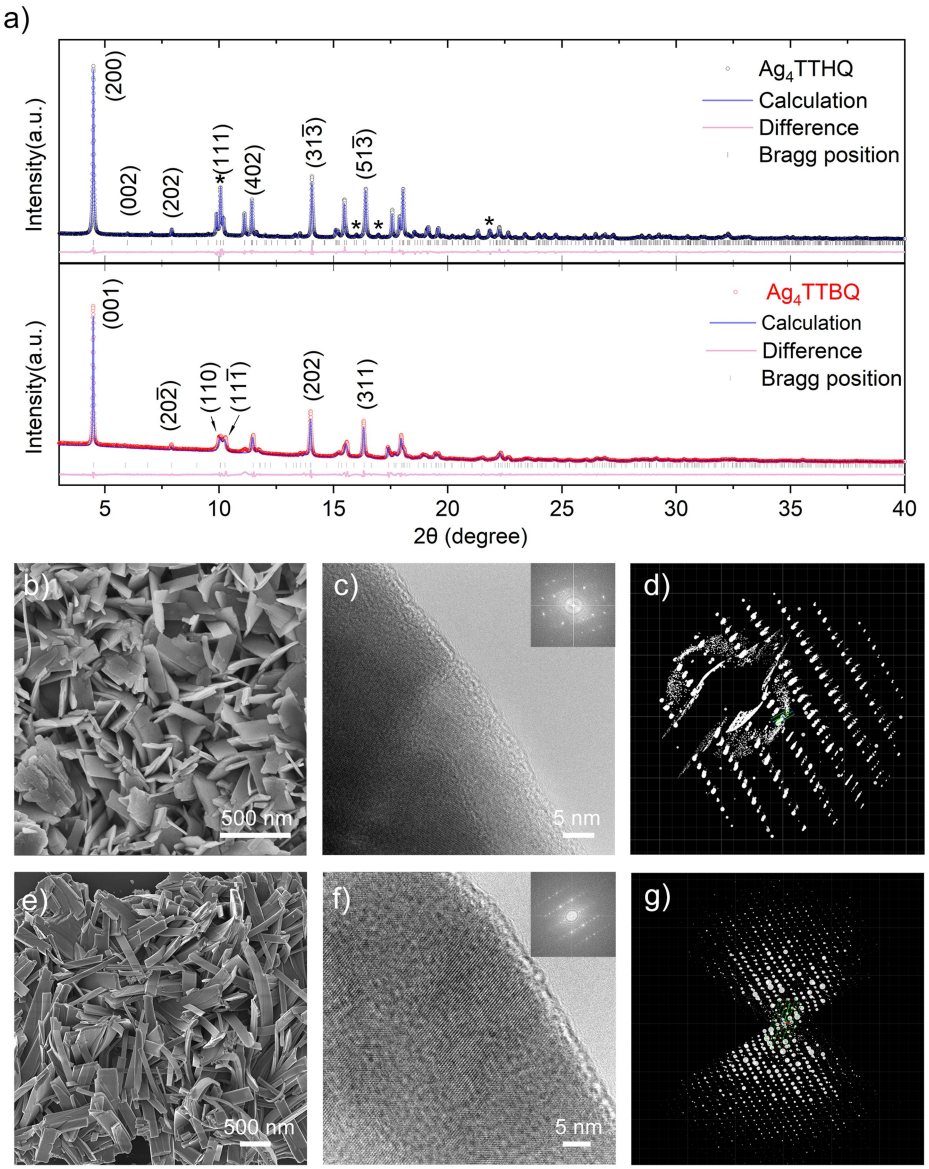

Figure 2. Characterization of crystallinity and morphology of Ag_4TTHQ and Ag_4TTBQ. (a) Rietveld refinement was performed on synchrotron radiation X-ray diffraction data for both Ag_4TTBQ and Ag_4TTHQ. Experimental data are shown in circles, and the calculated (blue) and difference (pink) curves are displayed from top to bottom. Gray vertical bars indicate Bragg positions. Peaks representing mismatches between Ag_4TTHQ and Ag_4TTBQ have been indicated with a star symbol. Scanning electron microscopy (SEM) image and high-resolution transmission electron microscopy (HRTEM) image of Ag_4TTHQ (b, c) and Ag_4TTBQ (e, f). The 3D reciprocal lattices of Ag_4TTHQ (d) and Ag_4TTBQ (g) resolved by Rotation Electron Diffraction are compared.

Ag_4TTHQ. There are several strong peaks in the low-angle range ($<10°$) that are well-aligned between Ag_4TTBQ and Ag_4TTHQ. However, noticeable peak distinctions persist, particularly in the higher angle range ($>15°$), indicating that they may have the same structural topology but exhibit non-negligible structural differences. Furthermore, the SEM images of Ag_4TTHQ (Figure 2b) and Ag_4TTBQ (Figure 2e) reveal that both compounds exhibit ribbon-like morphology with crystal sizes of hundreds of nanometers. Their highly crystalline nature is confirmed by the clear lattice fringes in their TEM images (Figures 2c and 2f). Interestingly, we found that the electron beam sensitivity of the Ag_4TTHQ sample is higher than that of Ag_4TTBQ. Loss of crystallinity caused by electron damage was observed within several minutes for Ag_4TTHQ, while Ag_4TTBQ maintained crystallinity for several hours under the same electron dose. These observations provide additional support for the presence of hydroxy groups in Ag_4TTHQ since hydroxy groups with attached protons are more sensitive to electron beams than carbonyl groups.[17] Moreover, as shown in Figures 2d and 2g, nanocrystals of Ag_4TTHQ and Ag_4TTBQ were subjected to continuous rotation electron diffraction (c-RED) measurements (Figure S2), which revealed their single-crystal structures due to high resolution above 0.7 Å (Figure S3). Thus, atomically precise structures were directly solved based on several datasets collected from different batches of

samples. Ag_4TTHQ was found to crystallize in a monolithic $C2/c$ space group with a unit cell of $a=17.828(4)$ Å, $b=4.2560(9)$ Å, $c=13.327(3)$ Å, $\alpha=90°$, $\beta=97.26(3)°$ and $\gamma=90°$, while Ag_4TTBQ crystallized in a monoclinic $I2/m$ space group with a unit cell of $a=10.340(2)$Å, $b=4.1709(8)$ Å, $c=11.940(2)$ Å, $\alpha=90°$, $\beta=105.16(3)°$ and $\gamma=90°$. The crystal cell size of Ag_4TTHQ is approximately twice that of Ag_4TTBQ, and its symmetry is lower than the latter. Further Rietveld refinement of the calcined structure against synchrotron PXRD data was performed (Figure 2a), providing more precise information on bond lengths and angles. The good refinement results obtained reveal high phase purity for both compounds. Details of the crystallography data (Tables S1, S2, S3, and S4) can be found in the Supporting Information.

Figure 3a presents the formation of bonds around the ligands in the crystal structures of Ag_4TTBQ and Ag_4TTHQ. Each ligand coordinates with ten silver atoms by bonding to sulfur and oxygen atoms in both Ag_4TTBQ and Ag_4TTHQ. The silver atoms are classified into two types, Ag1 and Ag2, based on their coordination geometry. Ag1 exhibits a distorted dodecahedron coordination geometry, while Ag2 has a capped dodecahedron geometry (Figure S4). Characteristic vibration signals of the Ag–Ag bond at around 150 cm^{-1} have been observed in the Raman spectra of Ag_4TTBQ and Ag_4TTHQ (Figure 1f). These two types of silver atoms interconnect through Ag–Ag bonds and sulfur bridge atoms to form 2D Ag–S networks, which have been shown to serve as highly efficient charge transport pathways.[18]

As shown in Figures 3b and 3c, the inorganic layers are separated by π-stacking columns of organic HQ/BQ units, making Ag_4TTBQ and Ag_4TTHQ organic-metal chalcogen (OMC) materials.[19] OMC materials feature strong orbital hybridization through covalent bond formation between their inorganic and organic components, offering a route to modify the electronic band structure by leveraging this hybrid structure. Despite having similar structure topology and inorganic structure motifs, Ag_4TTHQ and Ag_4TTBQ differ in their organic components. In Ag_4TTBQ, the bond

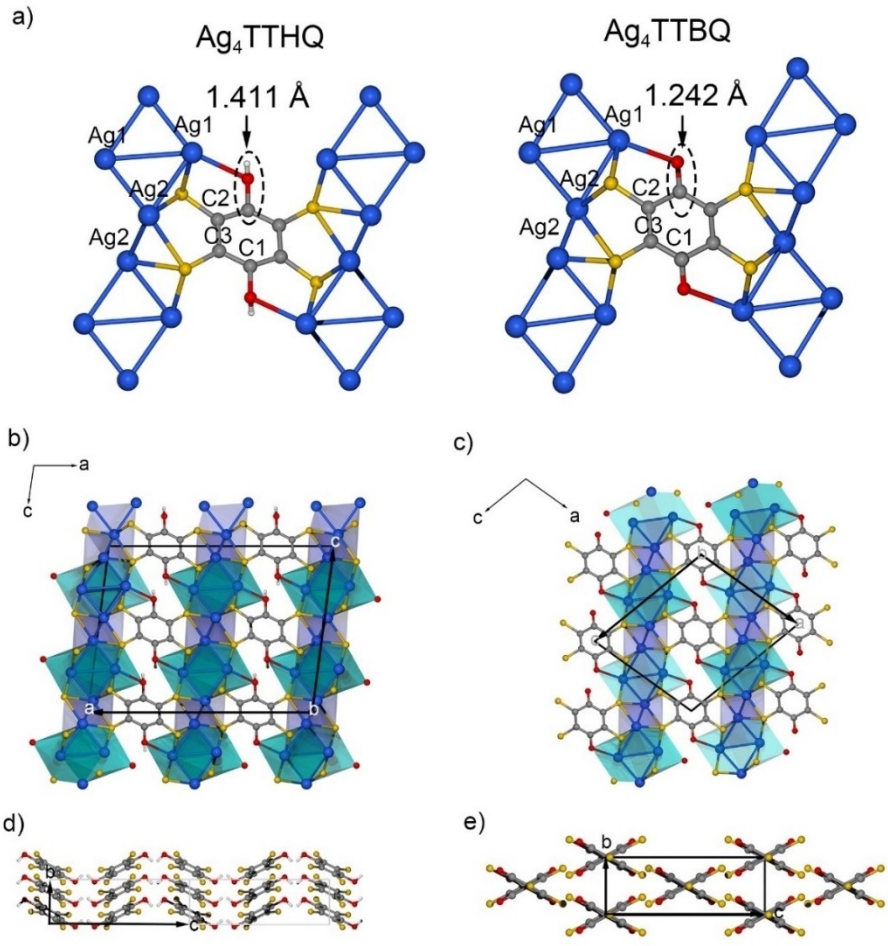

Figure 3. Comparison of the single crystal structures of Ag_4TTHQ and Ag_4TTBQ. (a) The complete coordination environment of each ligand in the structures of Ag_4TTHQ (left) and Ag_4TTBQ (right). Crystal structures viewed along the [010] direction for Ag_4TTHQ (b) and Ag_4TTBQ (c), respectively. The blue and purple polyhedra represent the Secondary Building Units (SBU) of two different Ag centers with distinct crystallographic features. These SBUs are interconnected to form an extended inorganic layer. (d) and (e) show the ligand packing modes for Ag_4TTBQ and Ag_4TTHQ, respectively, viewed through the [100] direction, with metal ions omitted for clarity. Carbon is represented by grey, sulfur by yellow, oxygen by red, and silver by blue.

length of C=O is 1.242 Å (Figure 3a), which is consistent with a double bond. In contrast, the bond length of C–O in Ag-TTHQ is 1.411 Å (Figure 3a), indicating a single bond. These structural differences explain the C=O signal observed in the IR and Raman spectra of Ag_4TTBQ. We calculated the molecular orbitals of isolated single molecular motifs based on the crystal structures of Ag_4TTBQ and Ag_4TTHQ, as depicted in Figure S5. This analysis reveals that, following orbital hybridization, the Ag_4TTBQ motif exhibits a significantly lower LUMO level than Ag_4TTHQ. Thus, we anticipated that the transition from HQ to BQ would trigger the band structure evolution.

To elucidate the influence of HQ/BQ on the electronic band structure of c-CPs, we conducted electronic band structure calculations based on their crystal structures. The calculated band diagrams (Figures 4a and 4b) show that Ag_4TTBQ and Ag_4TTHQ are non-degenerate semiconductors with distinct band gaps. Notably, the band gap of Ag_4TTHQ is found to be 1.5 eV, while that of Ag_4TTBQ is approximately 0.3 eV. In Ag_4TTBQ, we observed an additional conducting band (CB) above the Fermi level compared to Ag_4TTHQ, leading to a narrower band gap. To understand the origin of this additional band in Ag_4TTBQ, we dissected the total density of states (TDOS) into various orbital contributions, as shown in the right panels of Figures 4a and 4b. This analysis reveals a significant contribution of the *p* orbitals (p_x, p_y, and p_z) of O atoms to the additional CB band formed in Ag_4TTBQ (detail in Figure S6), highlighting the key role of the ligand oxidate state in determining the electronic band structure. Given these clues, we infer that the lowered LUMO level of TTBQ aligns more effectively with the *d* orbitals of silver and that this alignment fosters the formation of a new energy band near the Fermi level, thereby reducing the band gap. According to the calculated electronic band structures, strongly dispersive energy bands are observed along the Γ-Z and Γ-Y2 directions for Ag_4TTBQ and Ag_4TTHQ, respectively, indicating that efficient charge transport occurs parallel to the 2D Ag–S inorganic layer. The electron-hole reduced effective masses (m^*) are calculated to be 0.07 m_0 and 0.11 m_0 for Ag_4TTHQ and Ag_4TTBQ, respectively.

The large differences in electronic band structures inspire us to further explore the evolution of electrical and thermoelectrical properties. For that, we first use the parallel four-probe method to determine the temperature-dependent electrical conductivity (σ) of pellet samples of both materials (see Supporting Information for details). As shown in Figure 4c, the conductivity of Ag_4TTBQ is about 10 S/cm at room temperature, 25 times larger than Ag_4TTHQ (0.4 S/cm). The conductivities of both compounds increase with temperature. Given the polycrystalline nature of the pellets, we describe the temperature dependence of the conductivity using a model that considers both intra-crystal and inter-crystal transport[20](equation 1, Figure 4c and Figure S7):

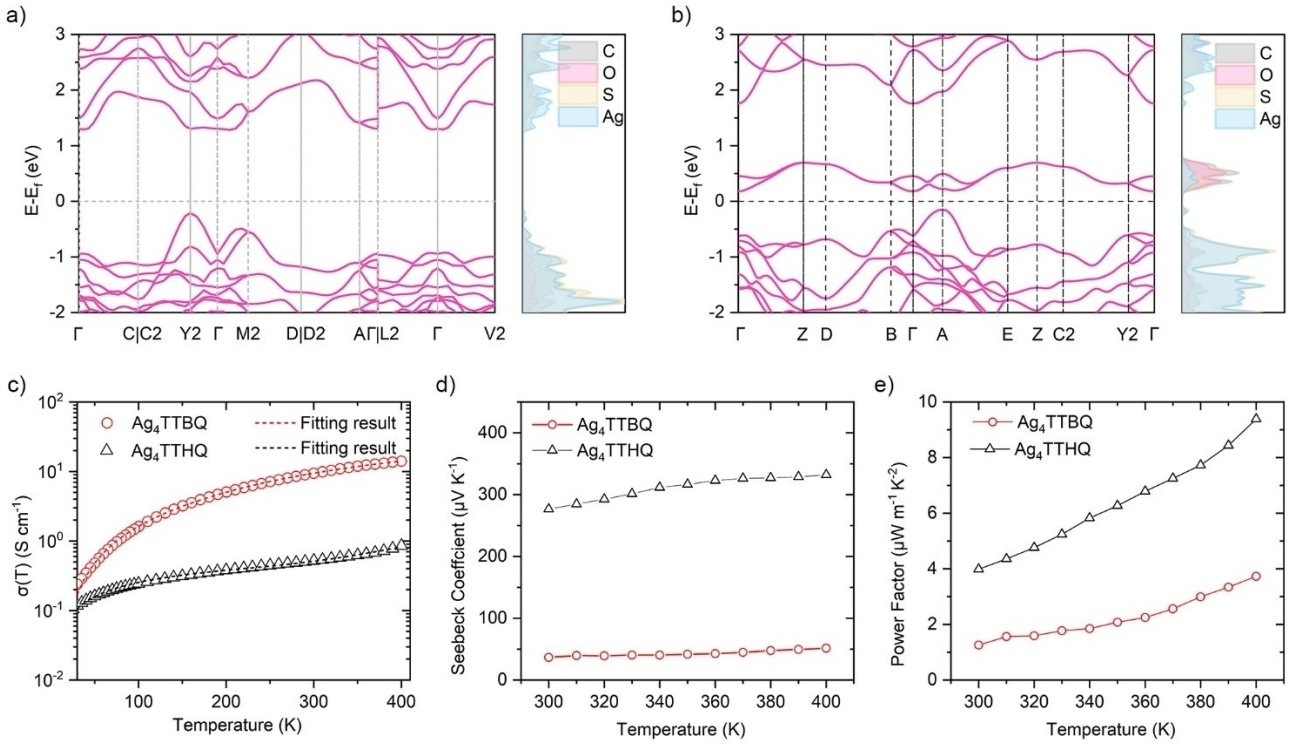

Figure 4. Electrical and thermoelectrical properties. (a) and (b) Band structures of Ag_4TTHQ and Ag_4TTBQ, respectively, based on their single crystal structures. The corresponding first Brillouin zone and high-symmetry K-points can be found in the Supporting Information. Electrical and thermoelectric properties of Ag_4TTBQ and Ag_4TTHQ as a function of temperature. (c) Electrical conductivity of Ag_4TTBQ and Ag_4TTHQ in the range of 10 K to 400 K. (d) Comparison of Seebeck coefficients and (e) power factors between 300 K and 400 K for Ag_4TTBQ and Ag_4TTHQ.

$$\sigma(T) = \sigma_0 \exp\left(-\frac{E_a}{k_B T}\right) + \sigma_h(T) \quad (1)$$

$$\sigma_h(T) = \sigma_1 \exp\left[-\left(\frac{T_0}{T}\right)^{1/4}\right] \quad (2)$$

where $\sigma(T)$ is the conductivity at temperature T, σ_0 is the pre-exponential factor, E_a is the activation energy, k_B is the Boltzmann constant, and $\sigma_h(T)$ is the contribution of inter-crystal transport. The first component of equation 2 represents the contribution of charge transport within the crystal driven by thermal activation. Our analysis, as depicted in Figure 4c and Figure S7, reveals the activation energies (E_a) of 0.18 eV for Ag_4TTHQ and 0.06 eV for Ag_4TTBQ. Notably, these values are lower than half of the band gaps, because the Fermi level is not at the center of the forbidden band for Ag_4TTBQ and Ag_4TTHQ. Moving to the second part of equation 2 ($\sigma_h(T)$), we delve into the realm of hopping transport, following the Various-Ranging Hopping (VRH) model.[20] This model elucidates how charge carriers traverse localized states within the band gap, hopping variably from one site to another. Here, σ_1 represents the pre-exponential factor while T_0 is the characteristic temperature for hopping transport. Our fitting results underscore that charge conduction in Ag_4TTBQ and Ag_4TTHQ arises from a mixture of intra-crystal thermally activated transport and inter-crystal hopping transport($\sigma_h(T)$). The narrowed band gap in Ag_4TTBQ reduces the energy barrier for thermally activated charge transport. As a result, Ag_4TTBQ exhibits higher electrical conductivity than Ag_4TTHQ, particularly at high temperatures where intra-crystal transport is dominant. As the temperature decreases, inter-crystal hopping transport plays a more significant role in charge transport, reducing the conductivity difference between Ag_4TTHQ and Ag_4TTBQ.

The difference in electronic structure between Ag_4TTHQ and Ag_4TTBQ also significantly influences their thermoelectric properties. First, we calculated the Seebeck coefficient of both materials based on the valence band (VB) at the Fermi level, using Onsager coefficients simulations with BoltzTraP2 (Figure S8).[21] We found that the Seebeck coefficient of Ag_4TTHQ is one order of magnitude larger than that of Ag_4TTBQ. To confirm this, we experimentally measured the Seebeck coefficients of pellet samples of both materials using a standard reference method. The details of this method and the thermoelectric device used are provided in the Supporting Information (Figure S9). Our measurements showed that the Seebeck coefficient of Ag_4TTHQ is 330 μV/K at 400 K, seven times greater than that of Ag_4TTBQ (Figure 4d), closely aligning with our theoretical calculations.

We further derive their power factor (PF), a crucial indicator for thermoelectric materials defined by the product of the square of the Seebeck coefficient(S) and the electrical conductivity(σ) (PF=$S^2\sigma$). Ag_4TTHQ shows a PF of 10 μW/m·K^2, which is an order of magnitude larger than that of Ag_4TTBQ (Figure 4e). It should be emphasized that Ag_4TTHQ also has the highest power factor among the reported silver-based CPs (Figure S10).

The dynamics and transport properties of photoinjected charge carriers in Ag_4TTHQ and Ag_4TTBQ were investigated using time-resolved terahertz spectroscopy (TRTS). In TRTS measurements (Figure S11), charge carriers are optically injected into the material by above-band gap excitation using an ultrashort 1.55 eV pulsed laser, and the transport properties are characterized by a freely propagating single-cycle THz field with a duration of ~1 ps. Figures 5a–b show the pump fluence-dependent THz photoconductivity dynamic of Ag_4TTHQ and Ag_4TTBQ film samples (drop-casted, detailed in Supporting Information), respectively. After photoexcitation, they exhibit a rapid rise in conductivity due to the photo-injection of conductive charge carriers. This is followed by photoconductivity decay with distinctly different characteristics: Ag_4TTHQ shows a pump fluence-independent decay rate (Figure 5c), while Ag_4TTBQ exhibits a higher decay rate at elevated pump fluence (Figure 5d). To elucidate their distinct photoconductivity decay behavior, their pump fluence-dependent frequency-resolved photoconductivity ($(\Delta\sigma(\omega))$) at 1 ps after the maximum photoconductivity was measured (Figure S12). We find that $\Delta\sigma(\omega)$ at varied pump fluences can be well described by the Drude–Smith (DS) model, where the motion of charge carriers is subject to backscattering (e.g., at grain boundaries), following:

$$\Delta\sigma(\omega) = \frac{\omega_p^2 \varepsilon_0 \tau}{1 - i\omega\tau}\left(1 + \frac{c}{1 - i\omega\tau}\right) \quad (3)$$

where ω_p is the plasma frequency, τ is the DS charge scattering time, and ε_0 is the vacuum permittivity. As summarized in Table S5, τ obtained at different pump fluences shows little variation within experimental error. This indicates that charge mobility can be considered constant over the range of carrier densities employed, allowing photoconductivity dynamics to be directly related to charge carrier population evolution. As exemplified in Figure 5e, the DS fits yield τ of 73 ± 4 and 76 ± 5 fs, and c of -0.93 and -0.89 for Ag_4TTHQ and Ag_4TTBQ, respectively. Knowing the effective masses from DFT calculations ($0.07\ m_0$ for Ag_4TTHQ and $0.11\ m_0$ for Ag_4TTBQ), the charge mobility of Ag_4TTHQ and Ag_4TTBQ are estimated to be 137 ± 7 and $130 \pm 9\ cm^2/(V \cdot s)$, respectively. The mobilities of Ag_4TTHQ and Ag_4TTBQ are well comparable to the state-of-the-art performance for 3D c-CPs (Table S6, Figure S13). To access the charge carrier decay rates associated with different recombination channels, we fit the pump fluence-dependent photoconductivity dynamics with the differential equation (Figures 5a and 5b, solid lines), following:

$$\frac{dn}{dt} = -k_1 n - k_2 n^2 \quad (4)$$

where $k_1$and k_2 represent the decay rates associated with trapping and bimolecular recombination,[22] respectively. We find that the essence of photoconductivity decay in

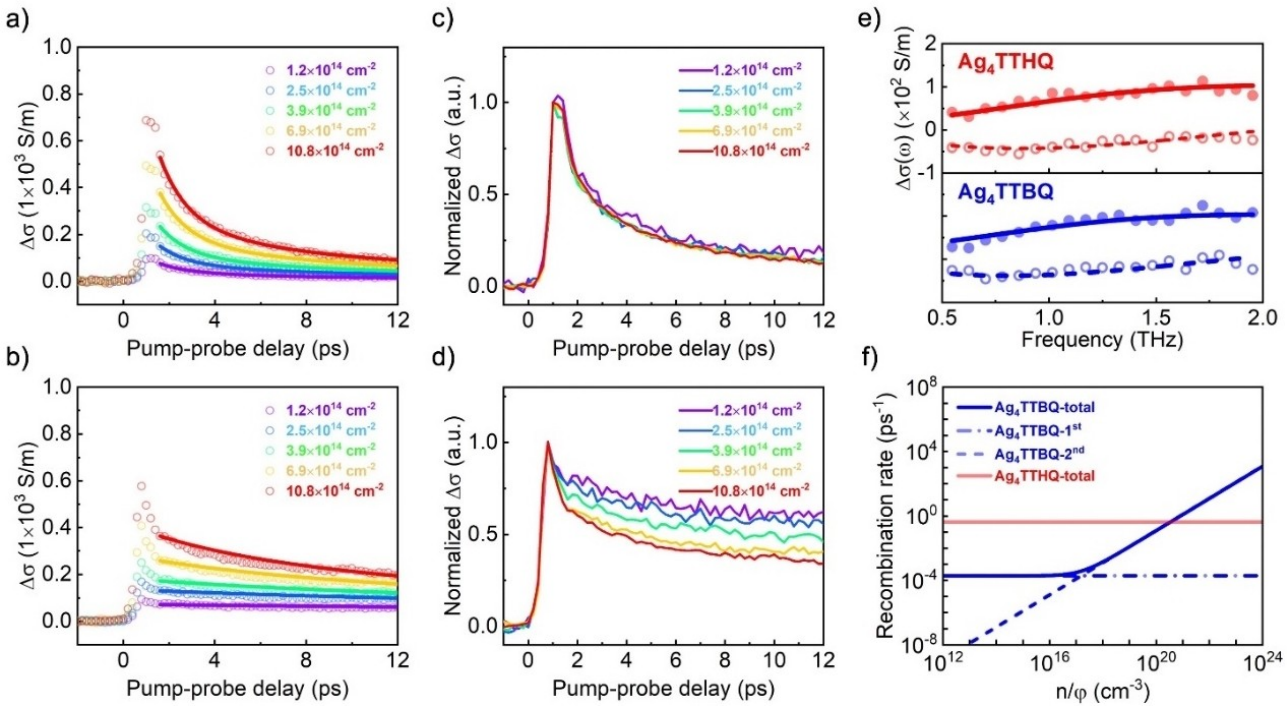

Figure 5. Microscopic charge transport properties. (a–b) Pump fluence-dependent photoconductivity ($\Delta\sigma$) dynamics for (a) Ag_4TTHQ and (b) Ag_4TTBQ. The solid lines are global fits to the coupled rate equations described in the main text. (c–d) Normalized pump fluence-dependent $\Delta\sigma$ dynamics for (c) Ag_4TTHQ and (d) Ag_4TTBQ. (e) $\Delta\sigma(\omega)$ for Ag_4TTHQ (upper) and Ag_4TTBQ (bottom) measured at 1 ps after the maximum photoconductivity. The solid and dashed lines correspond to the Drude–Smith fits to the real and imaginary parts of $\Delta\sigma(\omega)$. (f) Charge carrier recombination rates of Ag_4TTHQ and Ag_4TTBQ at varied carrier concentrations. Here, ϕ represents the photon-to-charge conversion ratio.

Ag_4TTHQ can be solely described by k_1 (Figure 5f, red solid line), indicating that trap-assisted recombination dominates the photoconductivity decay with a decay rate of 0.4 ps^{-1}. On the other hand, the photoconductivity decay in Ag_4TTBQ involves contributions from k_1 (Figure 5f, blue dotted line) and k_2 (Figure 5f, blue dashed line). The order-of-magnitude reduction of k_1 and the involvement of k_2 in Ag_4TTBQ suggests that defect-assisted recombination is largely suppressed, and intrinsic electron-hole recombination becomes the dominant recombination mechanism in the high carrier density region. These results demonstrate that the built-in hydroquinone/benzoquinone redox couple can significantly tune the electronic band structure while maintaining relatively high charge carrier mobility.

Conclusion

In this work, we demonstrate a novel synthetic strategy to tailor the electronic band structure and properties of semiconducting c-CPs. By using different metal sources to control the redox state of hydroquinone/benzoquinone ligands in the synthesis of c-CPs, we achieve precise control of the ligand oxidation state and electronic band structure without altering the topological networks. Our strategy is exemplified through the synthesis of Ag_4TTHQ and Ag_4TTBQ using different silver salts, which allows tuning of the band gap (from 0.5 eV to 1.5 eV) and conductivity (from 0.4 S/cm to 10 S/cm). DFT calculations reveal that these differences are due to the presence of energy bands near the Fermi level in Ag_4TTHQ and Ag_4TTBQ, enabled by the control exerted by HQ and BQ. Ultrafast THz spectroscopy reveals high charge carrier mobility above 100 $cm^2/(V\cdot s)$ for both compounds thanks to decent scattering times and relatively low effective masses. Notably, Ag_4TTHQ shows a high Seebeck coefficient of 330 μV/K and a power factor of 10 $\mu W/m\cdot K^2$, outperforming other reported silver-based c-CPs. Our findings highlight the potential of redox control in dictating the electronic band structure and properties of semiconducting c-CPs, which is critical to realizing the full potential of c-CPs in electronic and thermoelectric applications.

Acknowledgements

This work is financially supported by ERC starting grant (FC2DMOF, No. 852909), National Natural Science Foundation of China (22272092), ERC Consolidator Grant (T2DCP, No. 819698) and DFG projects (CRC-1415, No. 417590517; RTG 2861, No. 491865171). The authors acknowledge cfaed and the Dresden Center for Nanoanalysis (DCN) at TUD. R.D. thanks the Taishan Scholars Program of Shandong Province (tsqn201909047) and Natural Science Foundation of Shandong Province (ZR2023JQ005). W.X. acknowledges the financial support from the National

Natural Science Foundation of China (Grant 22071256 and 22379150). J.L. acknowledges the financial support from the National Natural Science Foundation of China (grant numbers: 22371121), the Fundamental Research Funds for the Central Universities of China (020514380306) and the Natural Science Foundation of Jiangsu Province (BK20230772) The authors also appreciate the crew of the BL14B1 beamline at the Shanghai Synchrotron Radiation Facility (SSRF) for their assistance in synchrotron PXRD data collection. The authors acknowledge Dr. Bo Guan and Dr. Xiang Hao from the Institute of Chemistry, Chinese Academy of Sciences for the measurements of rotation electron diffraction. P. St. P. is grateful to the European Union-NextGenerationEU, through the National Recovery and Resilience Plan of the Republic of Bulgaria, project No BG-RRP-2.004–0008 for the financial support and Discoverer PetaSC and EuroHPC JU for awarding access to Discoverer supercomputer resources.

Deposition Number(s) 2311803 (for Ag_4TTHQ), 2311802 (for Ag_4TTBQ), contain the supplementary crystallographic data for this paper. These data are provided free of charge by the joint Cambridge Crystallographic Data Centre and Fachinformationszentrum Karlsruhe Access Structures service. Open Access funding enabled and organized by Projekt DEAL.

Conflict of Interest

The authors declare no conflict of interest.

Data Availability Statement

The data that support the findings of this study are available from the corresponding author upon reasonable request.

Keywords: Conjugated coordination polymers · Metal–organic frameworks · Opto-electronics · Semiconductors · Benzoquinone

[1] M. Wang, R. Dong, X. Feng, *Chem. Soc. Rev.* **2021**, *50*, 2764–2793.
[2] M. Hmadeh, Z. Lu, Z. Liu, F. Gandara, H. Furukawa, S. Wan, V. Augustyn, R. Chang, L. Liao, F. Zhou, E. Perre, V. Ozolins, K. Suenaga, X. F. Duan, B. Dunn, Y. Yamamto, O. Terasaki, O. M. Yaghi, *Chem. Mater.* **2012**, *24*, 3511–3513.
[3] D. Sheberla, L. Sun, M. A. Blood-Forsythe, S. Er, C. R. Wade, C. K. Brozek, A. Aspuru-Guzik, M. Dinca, *J. Am. Chem. Soc.* **2014**, *136*, 8859–8862.
[4] T. Kambe, R. Sakamoto, K. Hoshiko, K. Takada, M. Miyachi, J. H. Ryu, S. Sasaki, J. Kim, K. Nakazato, M. Takata, H. Nishihara, *J. Am. Chem. Soc.* **2013**, *135*, 2462–2465.
[5] R. Dong, P. Han, H. Arora, M. Ballabio, M. Karakus, Z. Zhang, C. Shekhar, P. Adler, P. S. Petkov, A. Erbe, S. C. B. Mannsfeld, C. Felser, T. Heine, M. Bonn, X. Feng, E. Canovas, *Nat. Mater.* **2018**, *17*, 1027–1032.
[6] a) X. Huang, P. Sheng, Z. Tu, F. Zhang, J. Wang, H. Geng, Y. Zou, C. A. Di, Y. Yi, Y. Sun, W. Xu, D. Zhu, *Nat. Commun.* **2015**, *6*, 7408; b) X. Huang, S. Zhang, L. Liu, L. Yu, G. Chen, W. Xu, D. Zhu, *Angew. Chem. Int. Ed.* **2018**, *57*, 146–150.
[7] a) G. Givaja, P. Amo-Ochoa, C. J. Gómez-García, F. Zamora, *Chem. Soc. Rev.* **2012**, *41*, 115–147; b) L. Sun, M. G. Campbell, M. Dinca, *Angew. Chem. Int. Ed.* **2016**, *55*, 3566–3579; c) M. D. Allendorf, R. Dong, X. Feng, S. Kaskel, D. Matoga, V. Stavila, *Chem. Rev.* **2020**, *120*, 8581–8640; d) L. S. Xie, G. Skorupskii, M. Dinca, *Chem. Rev.* **2020**, *120*, 8536–8580.
[8] G. Wu, J. Huang, Y. Zang, J. He, G. Xu, *J. Am. Chem. Soc.* **2017**, *139*, 1360–1363.
[9] M. G. Campbell, S. F. Liu, T. M. Swager, M. Dincă, *J. Am. Chem. Soc.* **2015**, *137*, 13780–13783.
[10] X. Y. Song, X. Y. Wang, Y. S. Li, C. Z. Zheng, B. W. Zhang, C. A. Di, F. Li, C. Jin, W. B. Mi, L. Chen, W. P. Hu, *Angew. Chem. Int. Ed.* **2020**, *59*, 1118–1123.
[11] H. Arora, R. Dong, T. Venanzi, J. Zscharschuch, H. Schneider, M. Helm, X. Feng, E. Cánovas, A. Erbe, *Adv. Mater.* **2020**, *32*, 1907063.
[12] L. Sun, L. Yang, J.-H. Dou, J. Li, G. Skorupskii, M. Mardini, K. O. Tan, T. Chen, C. Sun, J. J. Oppenheim, R. G. Griffin, M. Dincă, T. Rajh, *J. Am. Chem. Soc.* **2022**, *144*, 19008–19016.
[13] X. Huang, Y. Qiu, Y. Wang, L. Liu, X. Wu, Y. Liang, Y. Cui, Y. Sun, Y. Zou, J. Zhu, W. Fang, J. Sun, W. Xu, D. Zhu, *Angew. Chem. Int. Ed.* **2020**, *59*, 22602–22609.
[14] a) T. Chen, J.-H. Dou, L. Yang, C. Sun, N. J. Libretto, G. Skorupskii, J. T. Miller, M. Dincă, *J. Am. Chem. Soc.* **2020**, *142*, 12367–12373; b) T. Kambe, R. Sakamoto, T. Kusamoto, T. Pal, N. Fukui, K. Hoshiko, T. Shimojima, Z. Wang, T. Hirahara, K. Ishizaka, S. Hasegawa, F. Liu, H. Nishihara, *J. Am. Chem. Soc.* **2014**, *136*, 14357–14360; c) L. Wang, A. Sarkar, G. L. Grocke, D. W. Laorenza, B. Cheng, A. Ritchhart, A. S. Filatov, S. N. Patel, L. Gagliardi, J. S. Anderson, *J. Am. Chem. Soc.* **2023**, *145*, 8486–8497; d) X. Huang, H. Li, Z. Tu, L. Liu, X. Wu, J. Chen, Y. Liang, Y. Zou, Y. Yi, J. Sun, W. Xu, D. Zhu, *J. Am. Chem. Soc.* **2018**, *140*, 15153–15156; e) Y. Sun, X. Huang, Y. Jin, Y. Li, Z. Li, Y. Zou, Y. Sun, W. Xu, *Inorg. Chem.* **2022**, *61*, 5060–5066; f) X. Sun, K.-H. Wu, R. Sakamoto, T. Kusamoto, H. Maeda, X. Ni, W. Jiang, F. Liu, S. Sasaki, H. Masunaga, H. Nishihara, *Chem. Sci.* **2017**, *8*, 8078–8085; g) T. Chen, J.-H. Dou, L. Yang, C. Sun, J. J. Oppenheim, J. Li, M. Dincă, *J. Am. Chem. Soc.* **2022**, *144*, 5583–5593.
[15] R. Dong, Z. Zheng, D. C. Tranca, J. Zhang, N. Chandrasekhar, S. Liu, X. Zhuang, G. Seifert, X. Feng, *Chem. Eur. J.* **2017**, *23*, 2255–2260.
[16] M. Tashiro, K. Koya, T. Yamato, *J. Am. Chem. Soc.* **1982**, *104*, 3707–3710.
[17] J. Li, C. Lin, T. Ma, J. Sun, *Nat. Commun.* **2022**, *13*, 4016.
[18] J. Wang, S. Fu, H. Zhang, R. Graf, H. Halim, S. Chen, W. Zheng, M. Bonn, K. Landfester, A. Riedinger, H. I. Wang, *Adv. Funct. Mater.* **2022**, *32*, 2113147.
[19] G.-E. Wang, S. Luo, T. Di, Z. Fu, G. Xu, *Angew. Chem. Int. Ed.* **2022**, *61*, e202203151.
[20] N. F. Mott, *Philos. Mag.* **1969**, *19*, 835–852.
[21] G. K. H. Madsen, J. Carrete, M. J. Verstraete, *Comput. Phys. Commun.* **2018**, *231*, 140–145.
[22] L. M. Herz, *Annu. Rev. Phys. Chem.* **2016**, *67*, 65–89.

Manuscript received: December 27, 2023
Accepted manuscript online: March 15, 2024
Version of record online: April 9, 2024